Impulse Response Modeling for Underwater Optical Wireless Channels

YIMING LI[1], MARK S. LEESON[2], AND XIAOFENG LI[1,*]

[1] School of Astronautics and Aeronautics, University of Electronic Science and Technology of China, Chengdu, Sichuan, 611731 China
[2] School of Engineering, University of Warwick, Coventry, CV4 7AL UK
*Corresponding author: lxf3203433@uestc.edu.cn

In underwater optical wireless communication (UOWC) channels, impulse response is widely used to describe the temporal dispersion of the received signals. In this paper, we propose a new function to model the impulse response in most realistic cases in the UOWC channels. By exploiting the inherent properties of such channels, our newly proposed model is superior to the conventional weighted double Gamma functions (WDGF) model in explaining the behavior of the channel. We use Monte-Carlo simulation to verify that our newly proposed model has a better accuracy of numerical fitting in most cases. Therefore, this new modeling approach offers a more convenient way to evaluate the performance of different kinds of UOWC channels. © 2018 Optical Society of America

1. INTRODUCTION

Underwater optical wireless communication (UOWC) systems have received a great deal of attention due to the advantages of a much higher data rate, security, and a much lower latency compared to the traditional underwater acoustic communication systems. Although the transmit length is relatively short as the light beam suffers from absorption, scattering and turbulence induced fading, UOWC is still a promising technology in many applications such as the underwater wireless sensor networks (UWSNs) to satisfy the increasing demands for ocean exploration with high data rate transmission [1].

Prior studies have shown that the optical beam will suffer from absorption and scattering, the properties of which can be described by the inherent optical properties (IOPs) of the water [2]. The absorption will cause an inevitable power loss and therefore the blue-green spectrum is used due to its minimum absorption by seawater. On the other hand, the scattering effect will change the direction of the transmit beams. In a turbid environment such as coastal and harbor waters, the photons will be undergo scattering more than once. This effect is called the multiple scattering effect which is studied in [3] and exerts a positive impact on the overall received power [4]. However, this effect will also increase the temporal dispersion which is a negative impact, particularly in very turbid water (e.g. harbor and coastal water).

On the other hand, the optical beam will also suffer from turbulence induced fading, which is caused by the random changes of water temperature and salinity, as well as the randomly distributed air bubbles in the water [5–10]. Moreover, experiments have shown that turbulence can be separated from particle scattering and absorption [11]. Therefore, it is reasonable to treat these two effects separately to reduce the complexity of the analysis.

In this paper, we focus on the temporal dispersion of the fading-free line-of-sight (LOS) UOWC channel and investigate the channel impulse response in turbid water. Recently, Monte-Carlo simulations have been carried out to analyze the properties of the impulse response in UOWC channels [12–15]. Furthermore, there has also been comparison of the Monte-Carlo results with Mullen's experimental study to validate the efficiency of the simulation results [13, 16]. Inspired by Mooradian's work on modeling the impulse response in clouds by the double Gamma functions (DGF), Tang applied the DGF to model the impulse response in UOWC links [17]. Moreover, Dong and Zhang modified the DGF model by adding parameters and terms to apply it to multiple-input-multiple-output (MIMO) UOWC channels [18, 19].

However, the channel properties of seawater differ from clouds to some extent. Therefore, we can observe a considerable degree of difference between the DGF model and the simulation results in Tang's work [17]. Although Dong and Zhang modified the DGF model by adding parameters and terms so that it thus better fits the simulation results, these models still did not explain the inherent properties of the impulse response in UOWC channels. Moreover, they added a number of parameters to be solved and thus severely degraded the efficiency of the

curve fitting process. To the best of our knowledge, no previous work has attempted to explain the connections between the IOPs and the impulse response models. In this work, we focus on explaining such questions and proposing a new model to fit the impulse response in most realistic situations. We also conclude by numerical results that the newly proposed model is superior to Dong's model in most cases. Moreover, we can also explain the similarities and differences of the impulse response in different types of water by the natural decomposition of absorption and scattering in our model. This provides a better approach to the estimation and analysis of the characteristics of UOWC channels.

This paper is organized as follows: Section 2 describes the optical characterizations and the scattering phase functions of seawater. In Section 3 we describe the basic rules of our Monte-Carlo simulation as well as discussing our newly proposed model. Simulation results and data analysis are presented in Section 4 followed by conclusions in Section 5.

2. PRELIMINARIES

A. Optical Characterizations of Seawater

According to Mobley's statement [2], absorption and scattering are two major effects in the underwater optical channel. The former will cause an inevitable loss of optical power by converting it into other forms such as heat. Meanwhile, the latter arises from the interaction of photons with the small particles in the water and will change the transmission path of the light. The energy loss caused by these two effects can be expressed by the absorption coefficient $a(\lambda)$ and the scattering coefficient $b(\lambda)$ respectively. Moreover, the attenuation coefficient $c(\lambda) = a(\lambda) + b(\lambda)$ is also defined to describe the overall energy loss in the channel. It is worth mentioning that the values of $a(\lambda)$, $b(\lambda)$ and $c(\lambda)$ will vary with the water type as well as the wavelength of the light λ.

B. Scattering Phase Function of Seawater

Unlike the optical wireless communication channel in the atmosphere, the light in the underwater optical channel will encounter a large number of particles and the scattering effect will be much more significant. As a consequence, multiple scattering effects will play a significant role in the received power. To study this kind of phenomenon, the scattering phase function (SPF) $\beta(\lambda, \theta, \phi)$ is introduced to describe the energy distribution of the scattering effect, where θ is the polar angle and ϕ is the azimuthal angle of the scattering respectively. The SPF is constrained so that:

$$\int_0^{2\pi} \int_0^{\pi} \beta(\lambda, \theta, \phi) \sin(\theta) \mathrm{d}\theta \mathrm{d}\phi = 1. \tag{1}$$

Moreover, it is often assumed that the particles are spherical and the scattering is azimuthally symmetric. Therefore, Eq. (1) can be rewritten as:

$$2\pi \int_0^{\pi} \beta(\lambda, \theta) \sin(\theta) \mathrm{d}\theta = 1, \tag{2}$$

where the 2π comes from the integral over the azimuthal angle.

Several models have been proposed to describe the SPF of the underwater environment. Among them there are two most widely used models.

The first is the long-standing Henyey-Greenstein phase function (HGPF) which was first proposed by Henyey to describe

the scattering effect in astrophysics [20]. This can be expressed as:

$$\beta_{HG}(\theta) = \frac{1 - g^2}{4\pi(1 + g^2 - 2g\cos(\theta))^{\frac{3}{2}}}, \tag{3}$$

where g is the average cosine of θ. Although this is very convenient for numerical calculation and acceptable to approximate the shape of the actual phase function in a multiple scattering channel, it differs from Petzold's long established measurements [21] in both small forward angles ($\theta < 20°$) and large backward angles ($\theta > 130°$) [22]. Therefore, use has been made of the Two-Term HGPF to improve the fitting performance. Although this does indeed enhance the fit, it also underestimates Petzold's measurement when $\theta < 1°$ because of the inherent property of such functions in small angle situations.

As a result, the HGPF has now been supplanted by the more complicated but more realistic and widley used Fournier-Forand phase function (FFPF). This was derived by Fournier and Forand as an approximate analytic form under two assumptions [23]. Firstly, the particles have a hyperbolic size distribution. Secondly, each particle scatters according to the anomalous diffraction approximation to the exact Mie theory. By applying the two approximations to the analytic form, the FFPF can also reveal some of the inherent properties of the underwater channel. The phase function is given by [24]:

$$\beta_{FF}(\theta) = \frac{1}{4\pi(1 - \delta)^2 \delta^\nu} \{\nu(1 - \delta) - (1 - \delta^\nu) \\ + [\delta(1 - \delta^\nu) - \nu(1 - \delta)] \sin^{-2}\left(\frac{\theta}{2}\right)\} \\ + \frac{1 - \delta_{180}^\nu}{16\pi(\delta_{180} - 1)\delta_{180}^\nu}\left(3\cos^2(\theta) - 1\right), \tag{4}$$

where $\nu = \frac{3 - \mu}{2}$ and $\delta = \frac{4}{3(n-1)^2}\sin^2\left(\frac{\theta}{2}\right)$. Here ν is the slope parameter of the hyperbolic distribution, n is the refractive index of the water, and δ_{180} is δ evaluated at $\theta = 180°$.

We illustrate the performance of the two models by comparison with the experimental data from Petzold's previous work [21]. Thus, the comparison of the HGPF, the FFPF and Petzold's experimental data is shown in Fig. 1. As may be seen in Fig. 1,
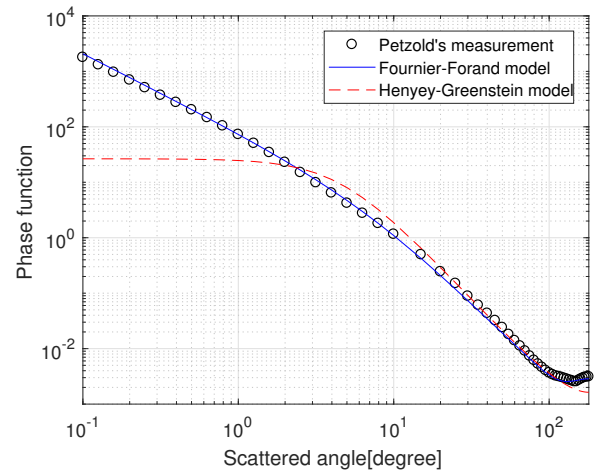

Fig. 1. Comparison of different phase functions.

the FFPF does a much better job of reproducing the shapes of

phase functions in the underwater environment than the HGPF, especially at very small angles. Therefore, we apply the FFPF to model the scattering effect in the rest of this paper.

3. IMPULSE RESPONSE MODELING

A. Monte-Carlo Simulation

To fully explore light propagation in the underwater environment it is necessary to solve the radiative transfer equation (RTE) [2]. Analytical solutions of the RTE are only available for a limited range of geometries and so Monte-Carlo Simulation is widely used to evaluate underwater channel performance. The method is much more convenient for application to the underwater environment given the paucity of analytical results for the RTE.

We adopt a Monte-Carlo approach similar to Cox and Tang's previous work [12, 17]. However, their modeling utilized the synthesis law of Poisson processes but violated the decomposition law of Poisson processes. Therefore, our Monte-Carlo simulation is modified in the transmission part to make it consistent with the definition of the absorption and scattering coefficients in [25]. On the other hand, we have also introduced some modifications in the receiving part to obtain a stabler result when analyzing the off-axis situation. The illustration of our system is shown in Fig. 2.
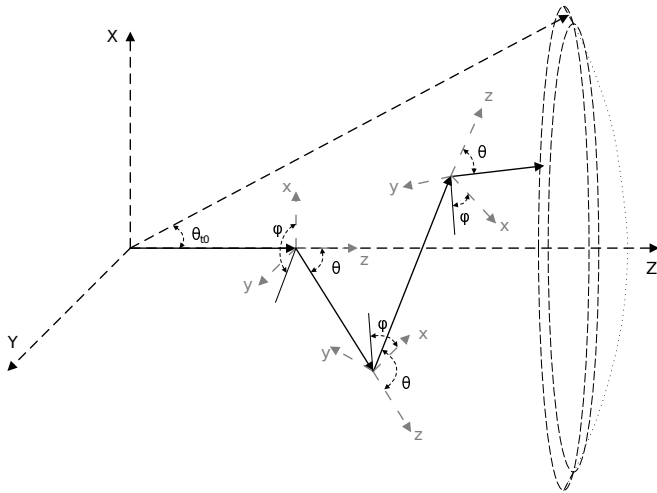

Fig. 2. The illustration of the Monte-Carlo Simulation.

The Monte-Carlo simulation of the system, which is illustrated in Fig. 2, is composed of three main parts: the initial part, the transmission part, and the receiving part.

In the initial part, we consider the collimated laser-based source. And the photon position is set at the origin of the Cartesian coordinates $(x_0, y_0, z_0) = (0, 0, 0)$ and the photon emission angle is set as $(\theta_0, \varphi_0) = (0, 0)$.

In the transmission part, the light will travel for a random distance obeying a negative exponential distribution, which can be expressed as:

$$p(\Delta s) = b \cdot e^{-b\Delta s}. \tag{5}$$

Therefore, the distance of the transmission path can be generated by:

$$\Delta s = -\frac{\ln(1 - U[0,1])}{b}, \tag{6}$$

where $U[0,1]$ is a uniformly distributed random variable.

Then the light will encounter a scattering effect. The zenith angle can be generated as follows. Firstly, the piecewise numerical approximation of the cumulative distribution function (CDF) $F_{FF}(\theta)$ can be calculated by using Eq. (4). Secondly, a uniform distributed random number $X \sim U[0,1]$ can be generated. Thirdly, we can generate the zenith angle by applying the equation:

$$\theta = F_{FF}^{-1}(X). \tag{7}$$

And the azimuth angle can be obtained by:

$$\varphi = 2\pi \cdot U[0,1]. \tag{8}$$

Meanwhile, the light will also suffer from the attenuation effect, and the power remaining before the nth scattering can be expressed as:

$$P_n = P_{n-1} \cdot e^{-a\Delta s}. \tag{9}$$

We should also transfer the zenith angle and the azimuthal angle into Cartesian coordinates. In this step, we allow as many as 300 scattering events to ensure that more than 99 percent of the paths are received in our simulation. Moreover, we have verified that this value is sufficient for all scenarios in this paper.

According to the analysis above, the absorption and the scattering effects have independent influences on the transmitted light. By distinguishing the differences between these two effects, we can analyze them separately in different steps. The first step is to construct the scattering path of the photon without considering the absorption effect. The second step is to calculate the absorption effect directly using the path length generated by the first step and Eq. (9). This will also influence our understanding of the impulse response modeling in Sec. 3 . B.

It is worth mentioning that the scattering path is determined by the scattering effect rather than the absorption effect. Inspired by this phenomenon, we introduce the term "scattering length" which is defined as bL in this paper. This is utilized to substitute the commonly used term "attenuation length" which is defined as cL, where L is the transmission distance between the transmitter and the receiver. In what follows, it is much more convenient to compare different water types by the application of this scattering length.

In the receiving part, we generalize the simulation and adapt it to both the on-axis and the off-axis situations. In order to achieve this goal, we have improved the structure of the simulation system which is shown in Fig. 2. Assuming the circular symmetric property of the azimuthal angle, we can collect all the photons reaching the receiving spherical surface with a radius of L and an off-axis zenith angle of $\theta_t \in [\theta_{t0} - \Delta\theta_{t0}, \theta_{t0} + \Delta\theta_{t0}]$ to estimate the performance of the receiver which is located at a distance of L and an off-axis zenith angle of θ_{t0} with a radius of $r0 = \Delta\theta_{t0}L$ (when $\theta_{t0} \leq \Delta\theta_{t0}$, the closed interval will be reduced to $[0, 2\Delta\theta_{t0}]$ and thus represent the on-axis situation). By applying this system, we can collect more photon paths when analyzing the off-axis situation so as to help us to obtain a stabler simulation result. It is worth mentioning that we should also normalize the receiver aperture when comparing the data. Moreover, only the photons within the receiving area as well as arriving from angles less than half of the receiver field-of-view (FOV) can be detected.

B. Functions for Impulse Response Modeling

Double Gamma functions (DGFs) have first been adopted to model the impulse response in clouds by Mooradian [26]. The form of such a function can be written as:

$$h(t) = C_1\Delta t e^{-C_2\Delta t} + C_3\Delta t e^{-C_4\Delta t}, \tag{10}$$

where C_1, C_2, C_3, and C_4 are the four parameters to be solved; $\Delta t = t - t_0 > 0$, where t is the time scale and $t_0 = L/v$ is the non-scattering propagation time which is the ratio of the link range L over the light speed in water v.

Inspired by the dispersive nature of both cloud and underwater channels, Tang applied double Gamma functions to model the impulse response in UOWC links [17]. However, such functions are only applicable with relatively large values of the attenuation length where the multiply scattered light is dominant. In order to generalize these functions, Dong added 2 parameters to the double Gamma functions and proposed the weighted double Gamma functions (WDGF) [18]:

$$h\left(t\right) = C_1 \Delta t^\alpha e^{-C_2 \Delta t} + C_3 \Delta t^\beta e^{-C_4 \Delta t}, \tag{11}$$

where α and β are the 2 newly added parameters to be determined. Eq. (11) is applicable for both small and large values of the attenuation length. Moreover, it is also applicable to model a 2×2 UOWC MIMO channel with a relatively large attenuation length. This function has also been extended to the general MIMO UOWC channel by Zhang [19].

However, by carefully inspecting the results of the Monte-Carlo simulation which is plotted on a logarithmic scale as Fig. 3, we can conclude that the tail of the impulse response should
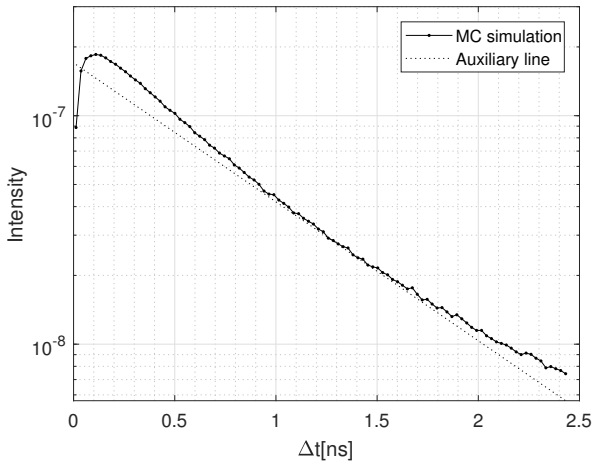

Fig. 3. Monte-Carlo simulation of impulse response in harbor water. L=10.93 m, FOV=40°.

be convex. This phenomenon implies that the tail decays more slowly than the exponential function. However, the weighted Gamma function is a strictly concave function. Although a fit can be made to the experimental data using Eq. (11), it will constantly underestimate the intensity of the tail because of this difference of convexity.

Inspired by the above mentioned problem, we propose a new function which can be written in the form of a combination of exponential and arbitrary power function (CEAPF) as below:

$$h\left(t\right) = C_1 \frac{\Delta t^\alpha}{\left(\Delta t + C_2\right)^\beta} \cdot e^{-a \cdot v\left(\Delta t + t_0\right)}, \tag{12}$$

where $C_1 > 0$, $C_2 > 0$, $\alpha > -1$, and $\beta > 0$ are the four parameters to be found and v is speed of light in water. To ensure that the function tends to 0 when Δt approaches infinity with arbitrary attenuation coefficient a we need to also apply the constraint $\beta > \alpha$. These parameters can be calculated from

Monte-carlo simulation results using the nonlinear least square criterion as:

$$(C_1, C_2, \alpha, \beta) = \arg\min\left(\int\left[h\left(t\right) - h_{mc}\left(t\right)\right]^2 \mathrm{d}t\right), \tag{13}$$

where $h\left(t\right)$ is the CEAPF model in Eq. (12) and $h_{mc}\left(t\right)$ is the results of the Monte-Carlo simulations.

It is easy to compare the CEAPF to the WDGF. Some of the most important conclusions are listed as below:

B.1. Convexity

We can rewrite Eq. (12) as:

$$\ln\left[h\left(t\right)\right] = \ln C_1 + \alpha \ln \Delta t - \beta \ln\left(\Delta t + C_2\right) - a \cdot v\left(\Delta t + t_0\right). \tag{14}$$

The second derivative of Eq. (14) is:

$$\frac{d^2 \ln\left[h\left(t\right)\right]}{\mathrm{d}\Delta t^2} = -\frac{\alpha}{\Delta t^2} + \frac{\beta}{\left(\Delta t + C_2\right)^2}. \tag{15}$$

When Δt is sufficiently large, which is the situation of the tail, CEAPF will be convex in accordance with the simulation result.

B.2. Decomposition of Absorption and Scattering

Since absorption and scattering are two independent effects in the underwater optical channel, the form of our newly proposed model naturally decomposes these two effects.

Absorption will convert optical power into other forms; this effect can be expressed by Eq. (9). By multiplying all the power loss of a certain trace, we can interpret the exponential term of Eq. (12) as the total loss of the trace.

On the other hand, the scattering effect will influence the distribution of the length of the received traces, and we can describe it by the arbitrary power term of Eq. (12). Specifically, C_1 describes the amplitude of the impulse response, the numerator of the term describes the rising edge and the denominator contributes to the falling edge of the function.

Moreover, by rewriting Eq. (12) as

$$h\left(t\right) = C_1' \frac{\left(b\Delta L\right)^\alpha}{\left(b\Delta L + C_2'\right)^\beta} \cdot e^{-\frac{a}{b} \cdot b\Delta L} \cdot e^{-\frac{a}{b} \cdot bL}, \tag{16}$$

where $\Delta L = v\Delta t$, $C_1' = (bv)^{\beta - \alpha} C_1$, and $C_2' = bvC_2$, we can compare different water types with the same scattering length. Firstly, although the distributions of the scattering path geometry are different with different scattering lengths, they will be similar with the same scattering length and thus the parameters of the arbitrary power term will be similar. This is in spite of the time dispersion typically being more pronounced with a longer scattering length due to the stronger multiple scattering effect and different parameter value solutions. It may be seen nevertheless, that value of the time dispersion Δt, which is proportional to ΔL, will be roughly inversely proportional to b as bL is a constant and L is proportional to ΔL with the same distribution of the scattering path geometry. Secondly, we can find that the value of $\frac{a}{b}$ in the second exponential term is responsible for the intensity of the received signal. Thirdly, we can conclude from the first exponential term that the suppression of the tail will be stronger with a clearer water type (i.e. with a larger $\frac{a}{b}$ ratio) when the scattering length is the same. Considering that the temporal dispersion is stronger with a greater scattering length (i.e. $\Delta L = v\Delta t$ is larger), we can also predict via this term that the suppression effect will be more pronounced as the scattering length increases.

B.3. Accuracy of the Estimation

By exploiting the inherent properties of the simulation results, we can expect a more accurate estimation than the WDGF model when applying our CEAPF model. As a result, when the multiple scattering effect dominates, and the transmit and receive apertures are precisely aligned, the performance of our newly proposed model is better in the sense of root-mean-square deviation (RMSE). Moreover, the CEAPF model will do a much better job when we are trying to predict the power in the tail.

Nevertheless, the CEAPF is also applicable for fitting the impulse response of a relatively smaller scattering length where the trajectory path still plays a significant role. Moreover, the CEAPF is able to accurately capture the off-axis behavior.

All the above mentioned scenarios are discussed in detail in Sec. 4.

B.4. Efficiency of the Estimation

Compared to the WDGF model with 6 parameters, the CEAPF model with 4 parameters can be computed more quickly when using the nonlinear least square criterion.

B.5. Integrability

In order to calculate the overall received power, we may need to integrate the CEAPF. By using Eq. (3.383.5.11) in [27], and then representing the Laguerre polynomials by confluent hypergeometric functions, which are standard built-in functions in most well-known mathematical software packages, given by:

$$_1F_1(a;b;z) = \sum_{n=0}^{\infty} \frac{a^{(n)}z^n}{b^{(n)}n!}, \qquad (17)$$

where $a^{(0)} = 1$ and $a^{(n)} = a(a+1)(a+2)\cdots(a+n-1)$ when $n \neq 0$, we can represent the overall received power as:

$$
\begin{aligned}
P = & C_1 e^{-aL} \cdot \pi \cdot \csc((\alpha - \beta)\pi) \\
& \cdot \left\{ \frac{C_2^{1+\alpha-\beta}\Gamma(1+\alpha)\,_1F_1(1+\alpha;2+\alpha-\beta;avC_2)}{\Gamma(\beta)\Gamma(2+\alpha-\beta)} \right. \\
& \left. - \frac{(av)^{-1-\alpha+\beta}\,_1F_1(\beta;-\alpha+\beta;avC_2)}{\Gamma(-\alpha+\beta)} \right\},
\end{aligned}
\qquad (18)
$$

where $\mathrm{Re}\{a\} > 0$, $\mathrm{Re}\{\alpha\} > -1$, and $\mathrm{Re}\{C_2\} > 0$. And all these constraints are consistent with our assumptions.

4. NUMERICAL RESULTS

We consider a UOWC system with 514 nm wavelength to correspond with that used in [21] and a photon detector with an aperture of 40 cm in diameter. Moreover, we choose a collimated source to receive the maximum power as would customarily be the case in experimental systems. On the other hand, we choose a typical value of $v = 2.237 \times 10^8$ m/s as the speed of light in water. The Monte-Carlo simulation is depicted in Sec. 3 . A; 10^9 transmissions are simulated to obtain the impulse response $h_{MC}(t)$ using MATLAB. Based on the settings above, we simulated the beam propagation for a range of link lengths, FOVs and off-axis angles in coastal ($a = 0.179\ m^{-1}$, $b = 0.220\ m^{-1}$) and harbor ($a = 0.366\ m^{-1}$, $b = 1.829\ m^{-1}$) water. We then produced a fit to the impulse response using Eq. (12) with the nonlinear least square criterion depicted by Eq. (13). The parameters of the CEAPF and WDGF are listed in TABLE 1 and TABLE 2 respectively.

Fig. 4 shows the normalized impulse response for FOV values of 20°, 40° and 180° in harbor water. Fig. 4 demonstrates

Table 1. parameters of CEAPF in different UOWC channels

FOV	C_1	C_2	α	β
L=5.47 m (bL=10), on-axis, harbor water.				
20°	5.244e-8	5.015e-2	-3.681e-2	3.019
40°	7.937e-7	2.957e-2	-3.595e-2	1.793
180°	1.390e-6	2.331e-2	-1.966e-2	1.564
L=10.93 m (bL=20), on-axis, harbor water.				
20°	1.677e-6	0.2730	0.6577	3.169
40°	1.320e-5	0.6657	0.4871	3.216
180°	9.072e-6	0.4374	0.4798	2.005
L=16.40 m (bL=30), on-axis, harbor water.				
20°	2.168e-6	0.6994	1.569	3.793
40°	3.207e-5	1.463	1.514	4.211
180°	2.236e-5	1.818	1.255	3.039
L=10.93 m (bL=20), off-axis angle=10°, harbor water.				
20°	9.653e-6	0.3661	3.947	7.765
40°	1.900e-4	0.8292	2.830	7.129
180°	2.800e-5	0.4760	3.007	5.183
L=45.45 m (bL=10), on-axis, coastal water.				
20°	4.888e-7	0.4169	-3.681e-2	3.019
40°	5.525e-7	0.2458	-3.595e-2	1.793
180°	5.754e-7	0.1938	-1.966e-2	1.564

that the CEAPF fits well with the simulated impulse response regardless of the propagation distance, FOV and off-axis angle. We set the bL product to be 10, 20 and 30, and these represented propagation distances of 5.47 m, 10.93 m and 16.40 m with on-axis impulse response results as shown in Fig. 4(a), (b) and (c) respectively. We can firstly conclude from these figures that the impulse response is more dispersive as L increases, which would be expected intuitively because the photons suffer more scattering over a longer propagation distance. Secondly, the impact of the FOVs will also increase with a larger L for the same reason. Thirdly, the received power will decrease with an increasing propagation distance as the photons undergo more attenuation. On the other hand, the impulse response of an off-axis angle of 10° is shown in Fig. 4(d). By comparing Fig. 4(b) and (d), we can also conclude that the impulse response disperses more heavily on an off-axis angle than an on-axis angle. Simultaneously, the received power will decrease on an off-axis angle due to the misalignment.

Moreover, in a typical situation of turbid water with a relatively long transmission distance of 10.93 m and a relatively small receiver FOV of 20°, a comparison between our result and the WDGF fitting result given by Eq. (11) is shown in Fig. 5. We can conclude from Fig. 5 that in such a situation, the CEAPF model performs better than the WDGF model, especially in the "tail" area. This result is in accordance with our analysis in Sec. 3 . B. Although this phenomenon is not always pronounced enough to be shown in figures, we can numerically compare our results with the WDGF fitting results. On one hand, We apply the rooted-mean-square deviation (RMSE) criterion, which is also used in Tang's previous work [17], to compare the overall performance. The RMSE criterion can be written as:

$$RMSE = \sqrt{\sum_{n=1}^{N}\left[h(t_0 + n \cdot \Delta t_0) - h_{mc}(t_0 + n \cdot \Delta t_0)\right]^2}, \qquad (19)$$

(a) L=5.47 m (bL=10), off-axis angle=0°

(b) L=10.93 m (bL=20), off-axis angle=0°

(c) L=16.40 m (bL=30), off-axis angle=0°

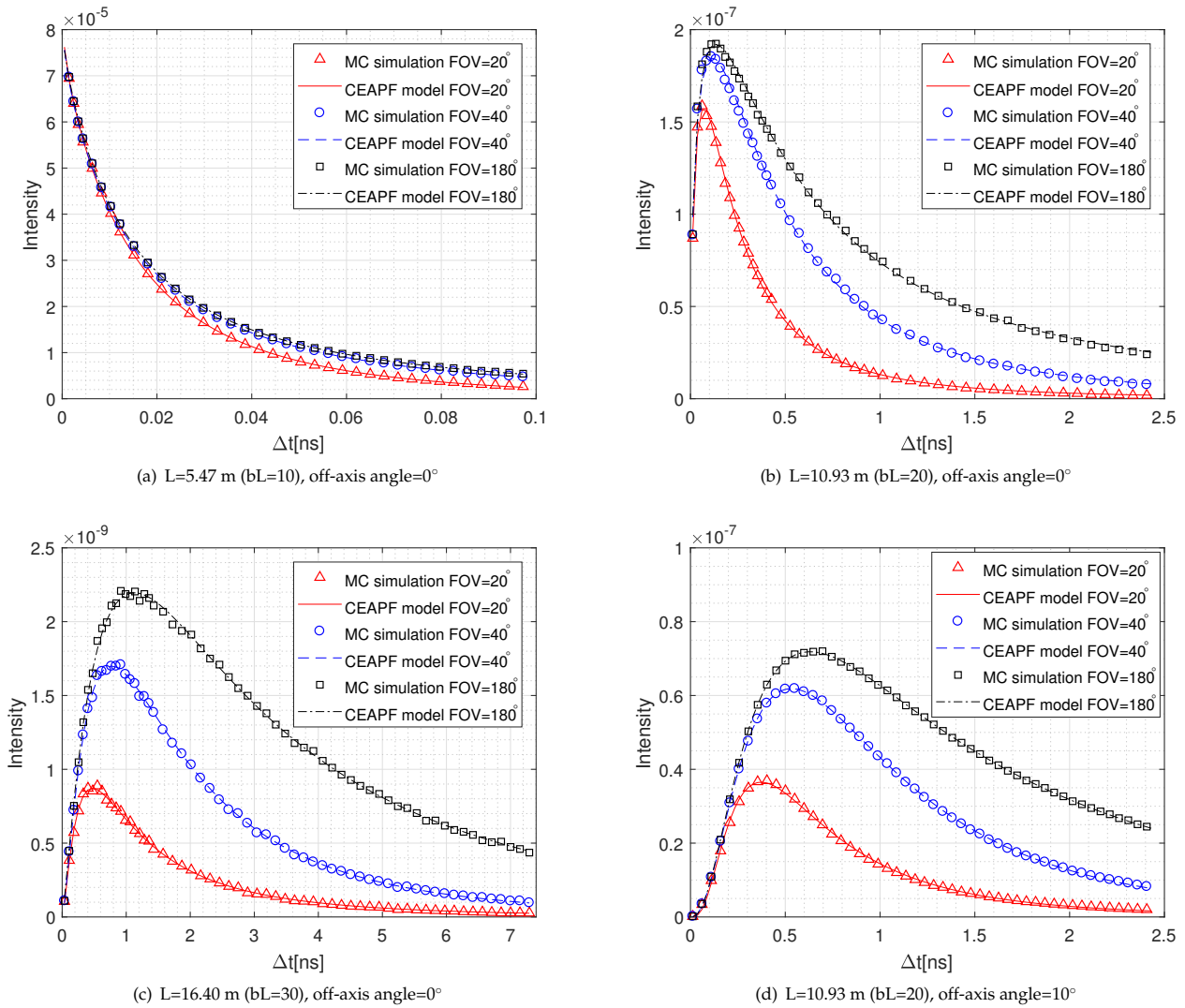(d) L=10.93 m (bL=20), off-axis angle=10°

Fig. 4. Impulse response in harbor water.

where Δt_0 is the unit time interval, N is the number of time intervals, $h_{mc}(\cdot)$ represents the impulse response obtained by Monte-Carlo simulation, and $h(\cdot)$ represents Eq. (11) when applying the WDGF and Eq. (12) when applying the CEAPF. On the other hand, in order to emphasize the improvement in estimating the tail of the impulse response, we also compared the power deviation of the tail (PDT), which can be written as:

$$PDT = \frac{P_{tail,h} - P_{tail,MC}}{P_{tail,MC}} \times 100\%, \tag{20}$$

where P_{tail} represents the overall power of the tail which is beyond the scope of the figures, $P_{tail,h}$ is calculated from the fitting curve, and $P_{tail,h}$ is calculated from the Monte-Carlo simulation result. The numerical results corresponding to Fig. 4 are listed in TABLE 3. We can conclude from TABLE 3 that the CEAPF model is better in most listed cases in the sense of RMSE. But the numerical data of Fig. 4(a) shows that the performance of the CEAPF model is slightly worse than the WDGF model in the sense of RMSE, but both error values are very small ($\leq 0.36\%$), effectively negligible. On the other hand, the numerical data of Fig. 4(d) shows that the performance of the CEAPF model

is slightly worse only in the case of $FOV = 20°$. As a result, the maximum RMSE deviations of the CEAPF model and the WDGF model are 1.03% and 1.34% respectively in all the cases listed in this paper. Moreover, the RMSE deviation of the DGF model is reported to be less than 5% in Tang's previous work (the maximum deviation listed is 4.276%, which is much larger than the CEAPF model) [17].

Another significant advantage of our new model is that it significantly increases the accuracy when estimating the overall power of the tail which is beyond the end of the subfigures in Fig. 4. we designed our simulation to collect all the received optical power so that we can calculate the power of the tail. By comparing the experimental results with the calculation results of the CEAPF (given by Eq. (18)) and the WDGF (which can be easily calculated by exploiting the properties of the gamma functions), we can numerically compare the PDT using both models. These results are also listed in TABLE 3. We can easily conclude that the WDGF model severely underestimates the power of the tail, but the CEAPF model does a much better job, which is in accordance with our analysis in Sec. 3 . B. By exploiting the inherent property of the impulse response in the

Table 2. parameters of WDGF in different UOWC channels

FOV	C_1	C_2	C_3	C_4	α	β
L=5.47 m (bL=10), on-axis, harbor water.						
20°	3.67e-5	57.9	1.44e-5	17.5	-8.32e-2	3.21e-2
40°	3.09e-5	64.7	2.13e-5	15.7	-8.68e-2	3.88e-3
180°	3.17e-5	63.8	2.03e-5	13.8	-8.50e-2	3.89e-3
L=10.93 m (bL=20), on-axis, harbor water.						
20°	9.41e-7	8.68	1.49e-7	2.38	0.556	0.444
40°	6.06e-7	5.37	2.23e-7	1.67	0.474	0.461
180°	5.13e-7	4.51	2.02e-7	1.07	0.441	0.413
L=16.40 m (bL=30), on-axis, harbor water.						
20°	4.65e-9	2.45	5.13e-10	0.640	1.12	0.673
40°	6.44e-9	1.77	9.84e-10	0.575	1.24	0.890
180°	4.79e-9	1.30	1.36e-10	0.432	1.10	0.998
L=10.93 m (bL=20), off-axis angle=10°, harbor water.						
20°	4.36e-6	6.83	9.52e-8	2.35	2.46	1.84
40°	2.33e-6	4.73	1.65e-7	2.00	2.24	1.99
180°	1.84e-6	4.34	1.69e-7	1.49	2.17	1.82
L=45.45m (bL=10), on-axis, coastal water.						
20°	1.37e-9	7.00	4.22e-10	2.13	-8.32e-2	3.21e-2
40°	1.16e-9	7.82	6.61e-10	1.92	-8.68e-2	3.88e-3
180°	1.19e-9	7.70	6.31e-10	1.69	-8.50e-2	3.89e-3

Fig. 5. A comparison of CEAPF and WDGF. Harbor water, on-axis, L=10.93 m (bL=20), FOV=20°.

Fig. 6. Impulse response in coastal water. L=45.45 m (bL=10). on-axis.

UOWC system (which is described in Sec. 3. B), the CEAPF model outperforms the WDGF model in all the cases.

We also examined the impulse response in coastal water, with results that are shown in Fig. 6. The CEAPF model also fits well in this type of water. To compare the results with the harbor water situation, we have used an appropriate range of Δt values in Fig. 6 so that the similarities in curve shapes between Fig. 4(a) and Fig. 6 (which have the same bL values) may be observed. Firstly, it is seen from the two figures that the intensity at the receiver is smaller in the coastal water situation. Seen from Eq. (16), we can find that the value of $\frac{a}{b}$ in the second exponential term is responsible for the smaller intensity. Moreover, the same receiver configuration will result in a smaller receive solid angle when the propagation length is larger in coastal water. Secondly, because of the same scattering length of $bL = 10$, both situations have similar scattering path distribution geometric at the scale of scattering length (this can be explained by the arbitrary power term in Eq. (16)). Nevertheless, the value of L and ΔL is larger in the situation of coastal water, resulting in a larger temporal dispersion as this is proportional to ΔL. By using the appropriate scale of the intensity and Δt in Fig. 6, we can find the shape of the impulse response is almost the same as Fig. 4(a). Actually, we can conclude from the numerical analysis that the impulse response decays slightly more quickly in the coastal water. This can be explained by the first exponential term in Eq. (16). Although $\Delta L = v\Delta t$ is too small to apparently change the shape, the bigger $\frac{a}{b}$ will result in a stronger suppression of the tail in coastal water.

5. CONCLUSIONS

In this paper, we have investigated the channel impulse response of fading-free LOS UOWC links due to the multiple scattering effect in different types of water. Inspired by the convexity of the simulation results in the logarithmic coordinate, we have presented a new function which can be written in the form
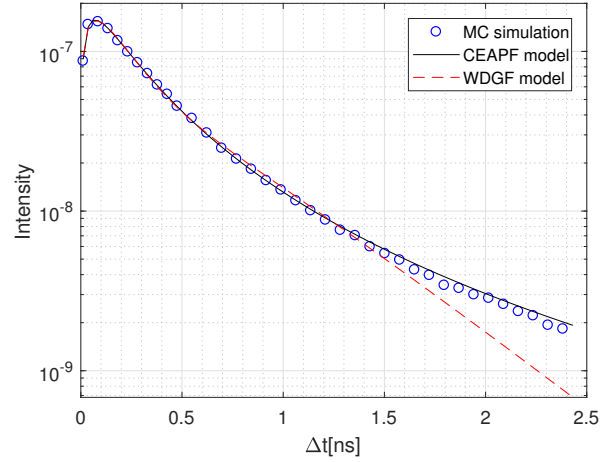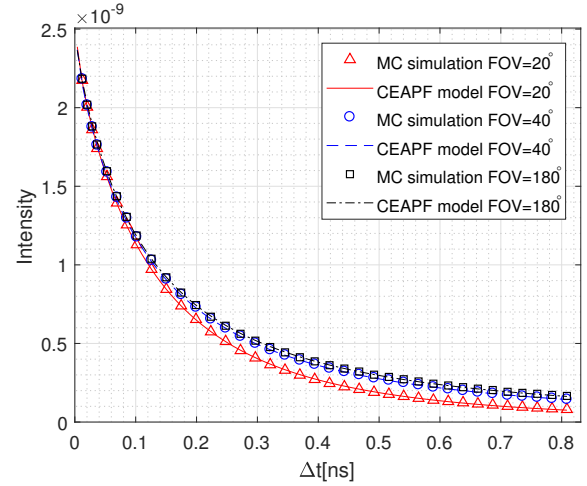
of a combination of exponential and arbitrary power function (CEAPF) to model the impulse response. This newly proposed model fits well with the simulation results and beats the widely used WDGF model in most cases according to the numerical analysis. This is particularly true when capturing the tail of the impulse response, where the CEAPF model reduces the power deviation in the tail by at least 20% and often more.

On the other hand, by naturally decomposing the two independent effects of absorption and scattering, we can use the newly proposed model to explain the similarities of the impulse responses in different types of water when the scattering length is the same.

Considering that the CEAPF model has fewer parameters to be solved, there are also some additional advantages such as a more efficient estimation with a shorter time consumption in parameter fitting. Based on all the analysis and results listed above, we can conclude that the newly proposed model is more efficacious than the conventional WDGF model. It provides a more convenient way to evaluate the performance of different kinds of UOWC systems.

Table 3. numerical performance comparison of CEAPF and WDGF in different UOWC channels.

RMSE			Power Deviation of the Tail		
FOV	CEAPF	WDGF	FOV	CEAPF	WDGF
L=5.47 m (bL=10), on-axis, harbor water.					
20°	0.18%	0.10%	20°	-13.65%	-28.65%
40°	0.36%	0.11%	40°	30.61%	-42.87%
180°	0.18%	0.11%	180°	15.25%	-54.48%
L=10.93 m (bL=20), on-axis, harbor water.					
20°	0.52%	0.95%	20°	15.19%	-87.59%
40°	0.92%	1.01%	40°	17.12%	-63.63%
180°	0.98%	1.15%	180°	34.84%	-55.12%
L=16.40 m (bL=30), on-axis, harbor water.					
20°	0.83%	1.34%	20°	-2.30%	-66.04%
40°	0.66%	0.93%	40°	-13.29%	-51.75%
180°	0.83%	1.05%	180°	5.54%	-39.71%
L=10.93 m (bL=20), off-axis angle=10°, harbor water.					
20°	1.03%	0.52%	20°	-36.62%	-64.70%
40°	0.39%	0.46%	40°	-24.06%	-49.61%
180°	0.30%	0.56%	180°	0.73%	-52.00%
L=45.45 m (bL=10), on-axis, coastal water.					
20°	0.18%	0.10%	20°	-13.58%	-27.40%
40°	0.36%	0.11%	40°	23.39%	-41.16%
180°	0.18%	0.11%	180°	8.51%	-51.32%

By applying this model to UOWC system, Our future work may be focused on the equalizer design of the high speed underwater wireless communication systems. Moreover, we may also carry out a research on estimating the performance of the underwater MIMO system by applying our model and analyzing each SISO sub-channel separately.

REFERENCES

1. Z. Zeng, S. Fu, H. Zhang, Y. Dong, and J. Cheng, "A survey of underwater optical wireless communications," IEEE Commun. Surv. & Tutorials **19**, 204–238 (2017).
2. C. D. Mobley, *Light and Water: Radiative Transfer in Natural Waters* (Academic Press, San Diego, CA, USA, 1994), 1st ed.
3. B. M. Cochenour, L. J. Mullen, and A. E. Laux, "Characterization of the beam-spread function for underwater wireless optical communications links," IEEE J. Ocean. Eng. **33**, 513–521 (2008).
4. B. Cochenour, L. Mullen, and J. Muth, "Temporal response of the underwater optical channel for high-bandwidth wireless laser communications," IEEE J. Ocean. Eng. **38**, 730–742 (2013).
5. M. V. Jamali, A. Mirani, A. Parsay, B. Abolhassani, P. Nabavi, A. Chizari, P. Khorramshahi, S. Abdollahramezani, and J. A. Salehi, "Statistical studies of fading in underwater wireless optical channels in the presence of air bubble, temperature, and salinity random variations (long version)," arXiv preprint arXiv:1801.07402 (2018).
6. D. K. Borah, A. C. Boucouvalas, C. C. Davis, S. Hranilovic, and K. Yiannopoulos, "A review of communication-oriented optical wireless systems," EURASIP J. on Wirel. Commun. Netw. **2012**, 91 (2012).
7. M. V. Jamali, P. Khorramshahi, A. Tashakori, A. Chizari, S. Shahsavari, S. AbdollahRamezani, M. Fazelian, S. Bahrani, and J. A. Salehi, "Statistical distribution of intensity fluctuations for underwater wireless optical channels in the presence of air bubbles," in "Communication and Information Theory (IWCIT), 2016 Iran Workshop on," (IEEE, 2016), pp. 1–6.
8. H. M. Oubei, E. Zedini, R. T. ElAfandy, A. Kammoun, M. Abdallah, T. K. Ng, M. Hamdi, M.-S. Alouini, and B. S. Ooi, "Simple statistical channel model for weak temperature-induced turbulence in underwater wireless optical communication systems," Opt. letters **42**, 2455–2458 (2017).
9. M. V. Jamali, J. A. Salehi, and F. Akhoundi, "Performance studies of underwater wireless optical communication systems with spatial diversity: Mimo scheme," IEEE Transactions on Commun. **65**, 1176–1192 (2017).
10. C. Wu, J. Ko, and C. C. Davis, "Imaging through strong turbulence with a light field approach," Opt. express **24**, 11975–11986 (2016).
11. C. Wu, J. R. Rzasa, J. Ko, D. A. Paulson, J. Coffaro, J. Spychalsky, R. F. Crabbs, and C. C. Davis, "Multi-aperture laser transmissometer system for long-path aerosol extinction rate measurement," Appl. Opt. **57**, 551–559 (2018).
12. W. C. Cox Jr, *Simulation, modeling, and design of underwater optical communication systems* (North Carolina State University, 2012).
13. J. Li, Y. Ma, Q. Zhou, B. Zhou, and H. Wang, "Channel capacity study of underwater wireless optical communications links based on monte carlo simulation," J. Opt. **14**, 015403 (2011).
14. A.-P. Huang and L.-w. Tao, "Monte carlo based channel characteristics for underwater optical wireless communications," IEICE Transactions on Commun. **100**, 612–618 (2017).
15. S. K. Sahu and P. Shanmugam, "A theoretical study on the impact of particle scattering on the channel characteristics of underwater optical communication system," Opt. Commun. **408**, 3–14 (2018).
16. L. Mullen, A. Laux, and B. Cochenour, "Propagation of modulated light in water: implications for imaging and communications systems," Appl. optics **48**, 2607–2612 (2009).
17. S. Tang, Y. Dong, and X. Zhang, "Impulse response modeling for underwater wireless optical communication links," IEEE transactions on communications **62**, 226–234 (2014).
18. Y. Dong, H. Zhang, and X. Zhang, "On impulse response modeling for underwater wireless optical mimo links," in "Communications in China (ICCC), 2014 IEEE/CIC International Conference on," (IEEE, 2014), pp. 151–155.
19. H. Zhang and Y. Dong, "Impulse response modeling for general underwater wireless optical mimo links," IEEE Commun. Mag. **54**, 56–61 (2016).
20. L. G. Henyey and J. L. Greenstein, "Diffuse radiation in the galaxy," The Astrophys. J. **93**, 70–83 (1941).
21. T. J. Petzold, "Volume scattering functions for selected ocean waters," Tech. rep., Scripps Institution of Oceanography La Jolla Ca Visibility Lab (1972).
22. C. Gabriel, M.-A. Khalighi, S. Bourennane, P. Léon, and V. Rigaud, "Monte-carlo-based channel characterization for underwater optical communication systems," J. Opt. Commun. Netw. **5**, 1–12 (2013).
23. G. R. Fournier and J. L. Forand, "Analytic phase function for ocean water," in "Ocean Optics XII," (International Society for Optics and Photonics, 1994), pp. 194–201.
24. G. R. Fournier and M. Jonasz, "Computer-based underwater imaging analysis," in "SPIE's International Symposium on Optical Science, Engineering, and Instrumentation," (International Society for Optics and Photonics, 1999), pp. 62–70.
25. C. Mobley, E. Boss, and C. Roesler, "Ocean optics web book," (2010).
26. G. C. Mooradian and M. Geller, "Temporal and angular spreading of blue-green pulses in clouds," Appl. Opt. **21**, 1572–1577 (1982).
27. A. Jeffrey and D. Zwillinger, *Table of integrals, series, and products* (Elsevier Inc., Burlington, MA 01803, USA, 2007), seventh ed.